Scanning Microscopy

Volume 7 | Number 1 Article 2

12-29-1992

Present Developments in Image Analysis

Peter Smart
Glasgow University

Xiaoling Leng
Glasgow University

Scanning Microscopy, Vol. 7, No. 1, 1993 (Pages 5-16) 0891-7035/93$5.00+.00
Scanning Microscopy International, Chicago (AMF O'Hare), IL 60666 USA

PRESENT DEVELOPMENTS IN IMAGE ANALYSIS

Peter Smart* and Xiaoling Leng

Civil Engineering Department, Glasgow University,
Glasgow, Scotland, G12 8QQ, U.K.

(Received for publication August 14, 1992, and in revised form December 29, 1992)

Abstract

The paper discusses novel methods of analysing oriented textures, explains some of the problems which had to be overcome to make these methods work, and indicates where future developments might be expected. This has required improvements in the methods of intensity gradient analysis, the development of large filter methods for mapping features defined in terms of their texture, and the introduction of ideas from the theory of regionalised variables.

Key Words: Soil, image analysis, intensity gradient, orientation, topcontouring, consistency ratio, semivariogram, mathematical morphology, density field mapping.

*Address for correspondence:
Peter Smart,
Civil Engineering Department,
Glasgow University,
Glasgow G12 8QQ, Scotland, U.K.
Phone No.: 44 (41) 339-8855

Introduction

This paper reports some methods of electron microscopy and of image analysis which have been developed to study the structures of clay soils either after deformation or in their natural state. Much clay consists almost entirely of extremely fine flat plates. These often come together face-to-face in sub-parallel groups called domains; random clusters of plates are also common; some soils also have loose single plate arrangements, large rounded particles amongst the clay, or large voids between the groups of particles. Typical structures are shown by Smart and Tovey (1981) and Grabowska-Olszewska *et al.* (1984); Bennett *et al.* (1991) place the work in context. The aim is to develop tools to analyse the structural arrangements in these soils quantitatively.

Virtually all of the electron microscope observations are now made using the back-scattered mode of scanning electron microscopy; but the methods have also been applied to ultra-thin sections, and some future use for fractured surfaces is foreseen.

The present samples are impregnated following the methods described by Smart and Tovey (1982). In brief, in the usual procedure, sub-samples are cut; the pore water replaced by acetone; the acetone by resin; the resin hardened; and plane surfaces carefully ground flat.

The scanning electron microscope images are digitised in the microscope; transmission electron micrographs can be digitised from negatives or, if necessary, from prints.

In the back-scattered mode, untilted samples are used. This presents a cross-sectional view of the sample, which simplifies the image analysis. Contrast in the back-scattered mode arises primarily from atomic number contrast, so that particles in general appear bright against a dark background of resin-filled pores. The incident electrons penetrate some distance into the sample, and there is some spreading of electrons within the sample before they escape back to the collector. Thus, some particles which are actually below the true surface may be seen more or less faintly; and there is also some softening of the contrast.

Figure 1 is a typical micrograph taken conventionally but at a lower magnification than usual. Low mag-

nifications are now being used experimentally in an attempt to widen the field of view. Results from a digitised version of Fig. 1 will be discussed below (Figs. 2-7). All our digitised micrographs are square with 512 rows of 512 pixels each and are digitised to 256 grey levels.

Before analysing the digitised electron micrographs, a number of steps were taken either to rectify defects in them or to eliminate defective micrographs. Much of this is common sense; but the reader is referred to the paper by Hounslow and Tovey (1992), which deals with the removal of the effect of electrical interference. This effect was discovered when blocks of plain resin were digitised. Hounslow and Tovey also used Wiener filtering to remove blur. Where they measured the point spread function from micrographs of small particles of dirt which were seen on plain resin blocks, we are attempting to measure it from micrographs of a glass-resin interface seen in cross-section. About 5 % of micrographs from a different source showed either missing scan lines or jumbling; and micrographs from a third source showed 'blips', which were discovered when a plain black field was digitised. Both the digitising apparatus and the monitor used for display must be calibrated in both directions.

Intensity Gradient Analysis

The electron micrographs show a planar cross-section through the material, in which most of the plates appear as thick lines. Apart from a few areas where the plates are jumbled together randomly, there is generally strong local preferred orientation; many of the micrographs also show an overall preferred orientation. Intensity gradient analysis (Unitt, 1975; Tovey *et al.* 1989a) is used to measure both the strength and direction of this overall preferred orientation.

In an electron micrograph showing bright particles against a dark background, the intensity gradient, grad I, is a vector, whose value is high at the edges of the particles, and whose direction is perpendicular to those edges. The analysis starts by calculating the intensity gradient:

$$\mathbf{U} = \text{grad } I \qquad (1)$$

$$U = \text{mod grad } I \qquad (2)$$

$$A = \text{arg grad } I \qquad (3)$$

Often, the 20,14-formula is used, because it appears to suit the work. This formula (see Appendix) uses the 20 nearest pixels and was derived from a least squares fit for the first 14 differential coefficients in a two dimensional Taylor series (full details of the derivation are available in Smart and Tovey, 1988). To avoid cases close to A = atan (0/0), pixels are labelled 'undecided' if U is smaller than an arbitrary limit, whose exact size seems to be of minor consequence. Following Tovey (1988), a threshold of 2 or 3 pixels is generally used.

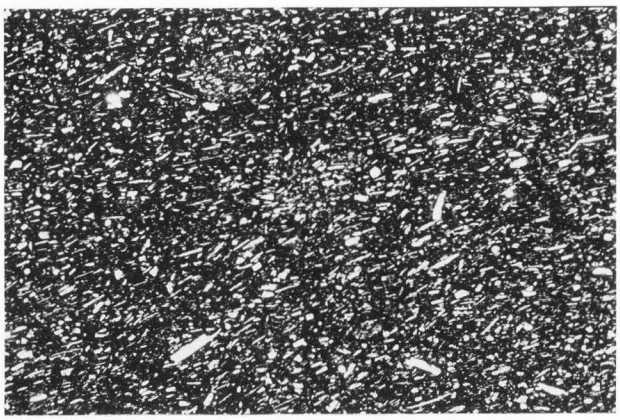

Fig. 1 (above). Back-scattered scanning electron micrograph of kaolin, zero tilt, ground section of impregnated sample. Photo width = 300 μm.

Figures 2-7 on facing page.

Fig. 2. Modified Chi-square vs. Filter Radius, for a typical micrograph.

Fig. 3. Average Consistency Ratio vs. Filter Radius for Fig. 1.

Fig. 4. Unweighted histogram of raw orientations, A, for Fig. 1; bin size is 1°; values for 181-360° are superimposed on those for 1-180°; vertical scale ‰ (parts per thousand); V = vertical, H = horizontal.

Fig. 5. Average Mean Vector, av mod **R**, vs. Orientation; bin size is 1°, vertical scale is arbitrary because mod **R** depends on the range of I.

Fig. 6. Unweighted histogram of smoothed orientations, T, for Fig. 1; bin size is 1°; range of T is 1-180°; vertical scale ‰.

Fig. 7. Average smoothed Porosity vs. Orientation for Fig. 1; bin size is 1°.

The choice of filters 5 pixels in diameter was guided by the rule that the resolution of a digitised image is twice the pixel spacing, so the microscopist should aim to use pixels one-fifth of the resolution which is desired. A check on the accuracy of the formulae for grad I was obtained by considering I to vary sinusoidally in one direction only. The results are shown in Table 1; note however that the 'more accurate' formulae have negative terms which at times reverse the direction of A, which is why the more robust empirical formulae suggested in Appendices 1 and 2 were invented.

The results of the intensity gradient analysis can be summarised in an unweighted rosette frequency histogram plot of orientation for each image. Earlier studies using this approach often gave spikey rosettes; but a combination of better digitisation, a more sophisticated formula, a better choice of the limit for the undecided case, and a more appropriate histogram bin size, have resulted in reasonably smooth rosettes. In some ways,

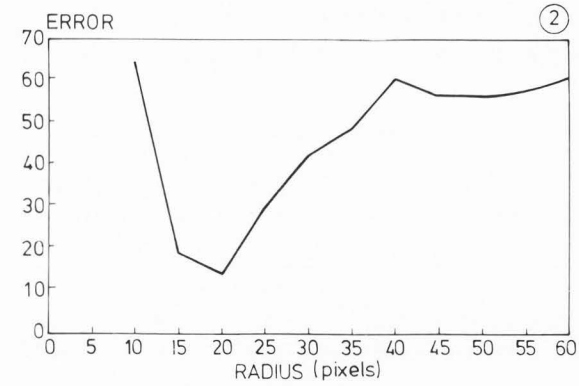
ERROR
2
70
60
50
40
30
20
10
0
0 5 10 15 20 25 30 35 40 45 50 55 60
RADIUS (pixels)

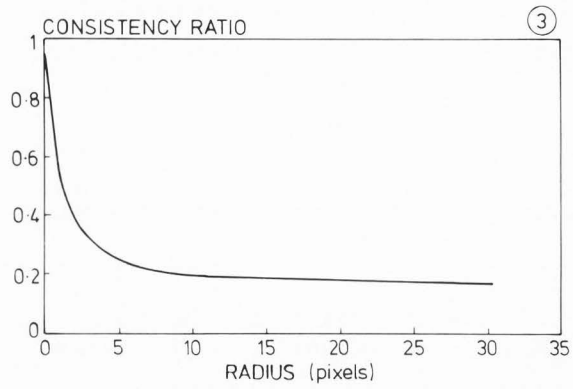
CONSISTENCY RATIO
3
1
0·8
0·6
0·4
0·2
0
0 5 10 15 20 25 30 35
RADIUS (pixels)

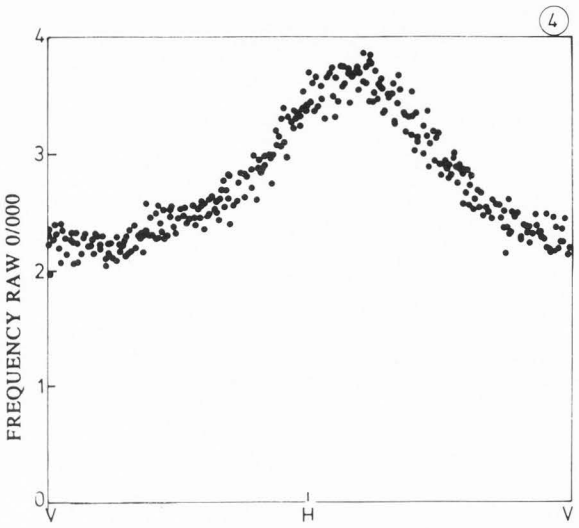
4
FREQUENCY RAW 0/000
4
3
2
1
0
V H V

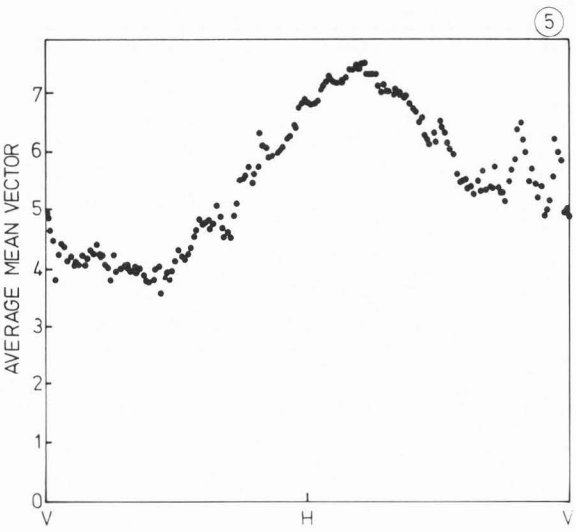
5
AVERAGE MEAN VECTOR
7
6
5
4
3
2
1
0
V H V

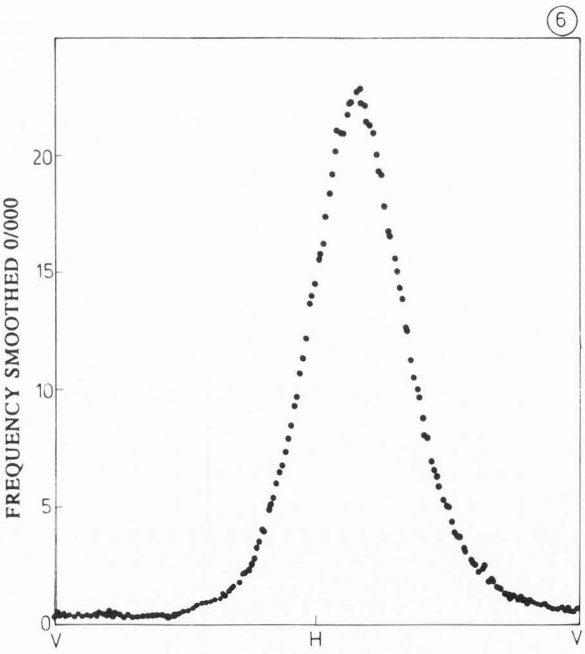
6
FREQUENCY SMOOTHED 0/000
20
15
10
5
0
V H V

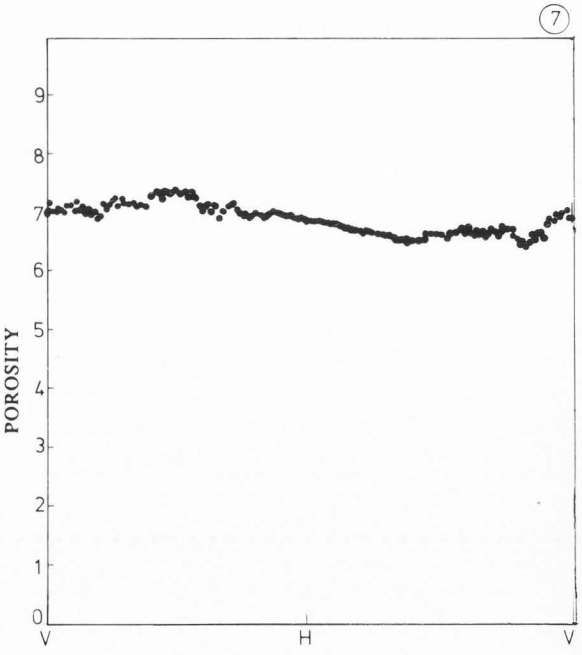
7
POROSITY
9
8
7
6
5
4
3
2
1
0
V H V

Appendix 1: Formulae for grad I, etc. 20,14-formulae.

The complete series of 20,14-formulae is obtained by transposition of the following, where the coefficients are in parts per thousand:

dI/dx

...	+013	...	-013	...
+077	-207	...	+207	-077
-070	-280	...	+280	+070
+077	-207	...	+207	-077
...	+013	...	-013	...

lap I

...	-035	+029	-035	...
-035	+284	+171	+284	-035
+029	+171	-1656	+171	+029
-035	+284	+171	+284	-035
...	-035	+029	-035	...

d^2I/dx^2

...	+053	-106	+053	...
-088	+142	-106	+142	-088
+135	+277	-828	+277	+135
-088	+142	-106	+142	-088
...	+053	-106	+053	...

$d^2I/dxdy$

...	+042	...	-042	...
+042	-417	...	+417	-042
...	...	...	...	...
-042	+417	...	-417	+042
...	-042	...	+042	...

d^3I/dx^3

...	+007	...	-007	...
-037	+047	...	-047	+037
-010	+060	...	-060	+010
-037	+047	...	-047	+037
...	+007	...	-007	...

d^3I/dx^2dy

...	+020	-040	+020	...
+060	-030	-060	-030	+060
...	...	...	...	...
-060	+030	+060	+030	-060
...	-020	+040	-020	...

d^4I/dx^4

...	-016	+033	-016	...
+025	-036	+022	-036	+025
-009	-061	...	-061	-009
+025	-036	+022	-036	+025
...	-016	+033	-016	...

d^4I/dx^3dy

...	000	...	000	...
-042	+083	...	-083	+042
...	...	...	...	...
+042	-083	...	+083	-042
...	000	...	000	...

d^4I/dx^2dy^2

...	+034	-068	+034	...
+034	-021	-026	-021	+034
-068	-026	...	-026	-068
+034	-021	-026	-021	+034
...	+034	-068	+034	...

Appendix 2: Empirical formulae for grad I

20T formulae

64 dI/dx

...	-1	...	+1	...
-1	-6	...	+6	+1
-2	-10	...	+10	+2
-1	-6	...	+6	+1
...	-1	...	+1	...

dI/dy by transposition; there are no others.

20S formulae

1000 dI/dx

...	-033	...	+033	...
033	-067	...	+067	+033
-034	-100	...	+100	+034
-033	-067	...	+067	+033
...	-033	...	+033	...

dI/dy by transposition; there are no others.

20U formulae

22 dI/dx

...	-1	...	+1	...
-1	-1	...	+1	+1
-1	-1	...	+1	+1
-1	-1	...	+1	+1
...	-1	...	+1	...

dI/dy by transposition; there are no others.

Table 1. Approximate errors in *U*.

Formula	%
Forward difference	10-47
4,2-formula	10
8,5-formula (Prewitt)	10
12,5-formula	25
12,9-formula (Unitt's)	1
20,5-formula	29
20,14-formula	1
24,5-formula	31-77
24,14	1
20U (see Appendix)	20-25
20S	21
20T	17
Sobell	10

an ordinary histogram (such as Fig. 4), is easier to interpret; this shows the preferred orientation of Fig. 1, which peaks at 15 degrees above the horizontal; directions here refer to the micrograph as printed. A wider bin size of 5 degrees would have smoothed away most of the scatter.

Mapping by Top-Contouring

As indicated above, the structure of clay soils often consists mainly of domains, i.e., groups of particles showing strong local preferred orientation, together with some random clusters of plates. In the past, these features had been mapped by hand; but now two new algorithms have been developed to map these features automatically.

The first of these new algorithms maps domains and random clusters by first encoding *A* into a limited number of directions, and then smoothing the encoded image (Smart *et al.*, 1988; Smart and Leng, 1990a, 1990b, 1991; Leng and Smart, 1991; also Tovey *et al.* 1989b, 1991, 1992). Typically, 4, 8, or 12 directions are used. The results may be presented: (**a**) by coloring each area on the map; (**b**) by superimposing boundaries on the original image; (**c**) by coloring the particles in the original image according to direction; (**d**) by ruling each area on the map; (**e**) by extracting each class in turn in a different image.

The encoded image is smoothed by selecting the most popular direction from the histogram of encoded angles within a large circular uniform filter. The filter is typically of 20 pixels radius, but this depends on magnification. Reflection is used to avoid leaving unprocessed borders. If more than an arbitrary number of pixels within the filter have undecided angles, then the pixel in the map is labelled undecided; by default, our code uses the radius of the filter as this limit, and, in the current work, it is rarely if ever exceeded. The pixel in the map is labelled 'random' if the difference between the maximum and the mean of the histogram is below a limit, EXC %, which may be set arbitrarily, but which is by default set by:

$$\text{EXC} = 200. * \text{SQRT}(-\text{LOG}(\text{PROB})/\text{NIF}) * \text{NOD} * \text{SIN}(\text{PI}/\text{NOD}) / \text{PI} \quad (4)$$

where NOD is the number of directions, NIF is the number of pixels in the filter, and PROB is the probability. Eqn. (4) is an approximation to Eqn. (11), see below.

The difference between the maximum and the mean is thought to be more robust than the difference between the maximum and the minimum in cases in which only one direction differs from the others.

As far as we know, no similar analysis had ever been reported; so some time was spent in testing the values of the various limits, in deciding the radius of the filter and how many directions to use, and in deciding the magnification and the other instrumental settings on the microscope.

The most difficult parameter to fix was the radius of the filter, because there was originally thought to be no predetermined optimum size for it. The only rule found was, in effect: to smooth away features of a given size, use a filter of a slightly larger size (see Grant *et al.*, 1990). In the main series of micrographs to be analysed, there were features of all sizes, so the initial choice of radius for the filter was made on the basis of visual assessment by a panel of experienced microscopists. For a series of micrographs at '2k x' magnification, the nominal radius chosen was 20 pixels; but the code increases the nominal radius by 0.4 pixels to improve the circularity of filters less than 8 pixels radius. Subsequently, a modified Chi-square test was used to test this choice. The image was mapped at various radii; the areas were averaged over all radii; and the sum of the squares of the errors of the original areas from the corresponding averages was treated as an error function. The result for a typical image of the series is shown in Fig. 2. The minimum at 20 pixels radius was encourging; and further support for this size of filter came from the analyses discussed below.

For cyclic data, top-contouring is the equivalent of the median filter used for ordinary data and is the proper choice of method for smoothing away very small features which are not wanted. Alternative approaches to mapping and analysis will be discussed below.

Consistency Ratio Mapping

Consistency ratio mapping is the second of the new algorithms to be developed for mapping clay structures. It is more accurate than topcontouring, about 15% slower using Occam2 and T800 transputers, and requires more memory; it maps domains and random clusters by first smoothing the vector field, **U**, then testing for randomness and segmenting the oriented areas into a limited number of equally spaced directions (Smart and Leng, 1990a; also Smart, 1991). The equations for the calculation within each filter are:

$$X = \Sigma\, U \cos 2A \quad (5)$$

$$Y = \Sigma\, U \sin 2A \quad (6)$$

$$S = \Sigma\, U \quad (7)$$

$$R = \surd (X^2 + Y^2) \quad (8)$$

$$C = R/S \quad (9)$$

$$T = \tfrac{1}{2} \text{ atan } (Y/X) \quad (10)$$

C is called the consistency ratio (see Smart and Tovey, 1982, Section 12.1.4 for a review). In general, pixels are mapped by segmenting the smoothed angle, T; however, if S is small, T must be labelled undecided and mapped accordingly, and if:

$$C < \surd \{(1/N) \ln (1/P)\} \quad (11),$$

where N is the number of (decided) pixels in the filter, and P is the probability of obtaining a greater consistency ratio by chance, then the pixel is mapped as random.

For analysing clay structure, the angle is multiplied by 2 at the start of the calculation and divided by 2 at the end, because the small linear features have two-fold symmetry (Smart and Leng, 1991, suggested extending the concept to chromatic mapping, which lacks this symmetry).

During these analyses, the program calculates C_{av}, the average value of C taken over all the filter positions in the image. Fig. 3 shows C_{av} versus (vs.) radius of filter for Fig. 1. If the filter radius is 0, C_{av} must be 1; as the radius increases towards infinity, C_{av} apparently tends to a limit; but for relatively small radii, the decrease towards this final trend line is rapid. It is thought that the point at which the curve straightens, at about 5 pixels, is the limit of local correlation between pixels, and that the corresponding radius may be the proper choice for the filters used above. Fig. 1 is at '400 x' magnification; so this result would have to be scaled up to 25 pixels radius at '2k x' magnification. Four versions of the algorithm exist. R may be used instead of C; and unweighted versions may be obtained by omitting U from Eqns. (5) and (6) and replacing S by N.

After the electron micrographs have been mapped, the mapped features are measured using standard routines. Only chord sizes need be considered here. The standard methods which are used in image analysis to measure features assume that all the features are comparable in size and that most of them lie wholly within the field of view. The maps produced here were more complicated. In some cases, they did conform to these assumptions; in other cases, there were very large domains which overlapped one or more edges of the micrograph. To obtain an alternative estimate of the sizes of the mapped features, the average chord size was calculated. The images are scanned from left to right. For each line, the average chord length is first obtained as usual discarding the incomplete chords at each end. Then, if these incomplete chords are larger than the average, they are brought back into the calculation. Thus, a global average for left-to-right scanning is obtained. The calculation is then repeated for top-to bottom scanning. It is now planned to add scanning along the diagonal directions. This method could be extended to measure each class of area separately.

Subsidiary Analyses

Introduction

In addition to the main set of algorithms developed in this study, several others were developed, assessed, or suggested; and these additional approaches are summarised below. In addition: Ross and Ehrlich (1991) applied pattern recognition techniques based on mathematical morphology to samples similar to those used here; and Derbyshire *et al.* (1992) used Fourier transforms to measure preferred orientation.

Enhanced orientation analysis

Intensity gradient analysis had originally been developed in soil microstructural analysis to measure the anisotropy of samples seen in scanning electron microscopes by obtaining the polar histogram of A. These were often almost elliptical, whereas Proctor (1977), whilst working with one of us, had shown that some at least of the hand mapping data followed semi-circular normal distributions. The consistency ratio mapping program was therefore modified to give an enhanced orientation analysis by providing histograms instead of maps (Leng and Smart, 1991). To illustrate the effect of this, Fig. 1 was processed using a radius of 6. The histogram of the smoothed orientation, T, Fig. 6, shows the preferred orientation more clearly than did Fig. 4. Histograms weighted by either R or C might also be used. Polar histograms of the smoothed angle, T, of some images show a few strong peaks, suggesting a multi-modal semi-circular normal distribution; those peaks which we have examined do seem to agree with subjective examination of the images, but see below. It is thought that the polar histogram of A is 'elliptical', because noise from the ends of the linear features and from other sources has degraded the 'true' distribution.

It is also possible to plot the strength of orientation against the direction of orientation, T. For example, Fig. 6 shows the average mean vector as a function of orientation. In calculating this figure, the values of mod **R** were summed for all pixels with the same value of T, taking a bin size of one degree, and the sum was divided by the number of pixels contributing to it. A similar calculation based on C is also possible. Fig. 5 suggests that when particles lie in the direction of preferred orientation, their parallelism is more perfect than that of particles lying in other directions. This type of diagram, which is obtained by division, seems to be less stable than diagrams obtained by averaging; small peaks, such as those on the right of Fig. 5, must be interpreted cautiously.

Hough transforms

The concept of multi-modal semi-circular normal distributions was given some support by an alternative analysis using Hough transforms after edge detection (Costa *et al.*, 1991a, 1991b). We have now developed a method of skeletonisation which works directly from the grey image as an alternative starting point; in addition, an anonymous referee suggested using the Hough transform itself directly from the original grey image.

Method of veins and convex hull

Some further support for the concept of multi-modal semi-circular normal distributions was given by a novel method of analysis, called the method of veins, which was invented by Daisheng Luo. In this method, the edges of the particles are followed and recorded as chain code; then, for each particle in turn, the chain code is reduced to provide a measure of the orientation of that particle (Lou *et al.*, 1992). Luo went on to analyse the particles by superimposing the convex hull, i.e., the figure formed by the enveloping tangents, from which he took the longest diameter as an indicator of orientation.

Enhanced orientation mapping

Rather than mapping the domains into predetermined directions, it would be preferable to map them into the directions indicated by the enhanced orientation analysis. At the time of writing, this is yet to be implemented; no difficulty is foreseen in choosing the directions interactively from the histogram of T, but the other histograms must be checked, and more experience is desirable before attempting to have the directions chosen automatically. It is thought that this method of enhanced orientation mapping may produce an extra class of area in which small packets of sub-parallel particles are mixed together randomly.

Semi-variogram

Complete semi-variograms for all lags up to one-quarter image size were calculated experimentally for a few micrographs following Webster and Oliver (1990), (see Smart and Leng, 1992; Smart *et al.*, 1992). The results were:

1). The range of the semi-variogram, which represents the average distance between two pixels which are quite unrelated to each other, appeared to be comparable to the size of the filter which had been selected for top-contouring and consistency ratio mapping.

2). The range of the semi-variogram varied in direction, thus giving for the first time, a definite indication of the ratio of the axes which should be used if the circular filter were to be replaced by an elliptical one.

3). Some long range order was apparent. This observation led to the development of the analysis described below under Density Field Mapping.

4). The nugget variance, i.e., the extrapolated variance at zero lag, was zero, suggesting that the magnification could have been lowered without serious loss of fine detail and with a gain in the size of the area examined. It would probably be necessary to adjust the aperture size (Tovey and Sokolov, 1981, Tovey *et al.*, 1992). It would almost certainly also be necessary to use a smaller filter when calculating grad I: to an extent, the present methods use double smoothing, once in the 5 x 5 filter for grad I, and later in the much larger circular filter; so this change would not be illogical.

Further work is proposed in this area to base the semi-variogram on grad I.

Density Field Mapping

By analogy with X-ray micro-analysis, the porosity, p, of an individual pixel is given approximately by:

$$p = (I_s - I)/(I_s - I_v) \qquad (12)$$

where I_s and I_v are the grey levels corresponding to pure solids and pure voids respectively. This method was developed for use in images in which the finest voids are smaller than the pixels with a view to measuring the porosity of each class of domain. The results quoted by Smart and Leng (1990a) for a mapped image were obtained in this way. If necessary, a gamma correction should be performed before making this analysis. Alternatively, if the magnification is reasonably high, the grey image may be segmented to black-and-white (see Hounslow and Tovey, 1992). Fig. 7 shows the porosity calculated from Equation (12) and smoothed using a filter of 6 pixels radius. The trend here seems to be the opposite of that of Fig. 5, i.e., better parallelism is accompanied by lower porosity; but this observation must not be taken as a general result, since some other observations appear to show the opposite.

After discovering long range order in the semi-variograms, a trial analysis of the variability of the density field was begun. Instead of density itself, the local porosity is being calculated by the grey level method within the same large uniform filter as is used for consistency ratio mapping. An intensity gradient analysis is made of the porosity field and compared with the results from the original intensity gradient method and from enhanced orientation analysis. To obtain the scale of the variation of porosity, the porosity field is segmented at the mean value for the sample, and a chord size analysis made. The porosity segments seem to be about twice as large as orientation segments mapped using four directions, which seems reasonable; and there are sometimes differences in strength and direction of orientation between the two fields, which again might have been expected (complete results will be reported by X. Bai in due course).

Large Voids

Smart *et al.* (1988) proposed to map large voids and large particles by erosion/dilation after grey level segmentation; the method is equally applicable to surfaces.

Fig. 8 shows a transmission electron micrograph of an ultra-thin section. The sample, which had been sheared, had failed along a plane; before impregnation, the sample had broken in two along this plane, which was well slickensided, i.e., polished. The micrograph shows a cross-section of this 'plane'; the direction of sliding was either left-to-right or right-to-left. Note some loose particles in the resin above the plane. Fig. 9 shows the surface obtained as follows: threshold (to get a black-and-white image); dilate the particles 16 pixels; erode 16 (surface located correctly, particles still there, sharp peaks on surface under particles); erode 10; dilate 10 (particles gone, peaks replaced by humps, see Fig. 10); dilate 3 (for safety); invert contrast; invert contrast of original; multiply (i.e., multiply pixel values and divide by maxgrey); invert contrast; threshold; dilate 17; erode 17; erode 10 (possibly unnecessary); dilate 10. The surface is now ready for analysis as suggested by Grant *et al.* (1990) and Smart and Leng (1992a). Fig. 10 shows an intermediate version of the boundary superimposed over the thresholded micrograph (add pixel values and divide by 2); views such as this were essential as checks.

Fig. 11 is a Consistency Ratio Map of Fig 8. The original micrograph was first masked by the final boundary, Fig. 8, after it had been dilated by two pixels. Then the contrast was adjusted to bring the resin as near zero as possible to minimise the effect of the truncation of the resin along the surface of the sample. The composite image was mapped using an arbitrarily chosen filter radius of 20 pixels and only four directional classes. This resulted in areas which overlapped beyond the surface of the sample by the radius of the filter; so the map was masked again using the undilated final boundary.

Fig. 12 illustrates an alternative view of the surface. The loose particles were masked out as above; then the cleaned image was thresholded. The surface was defined by traversing down the columns of pixels from the top until a particle was found. The resulting line follows the surfaces of the particles exactly but is broken at the steps.

Three-Dimensional Analysis

Most of the present samples are either axially symmetric or have a vertical plane of symmetry which can be recognised before impregnation; and often the objective is to distinguish between alternative models of behaviour between which discrimination can be made within the plane of symmetry. When a three-dimensional analysis is required, the best that can be done with these samples at present is to take observations from three mutually orthogonal surfaces, two vertical and one horizontal (this is a practical implementation of the Roscoe-Oatley proposal, which they made when first proposing the use of scanning electron microscopy for soils). The most important property of interest is the direction of the plane of preferred orientation. The observations on the three faces yield the orientations of the traces of this plane on these faces. When the plane of preferred orientation is sub-horizontal, its orientation can be found reasonably accurately from the traces on the two vertical faces alone. The general case is complicated by the need to adjust the observations, and several methods of adjustment are under consideration (Leng and Smart, 1992).

Further Analyses

Two further lines of enquiry have just begun. The structure of some clays is termed 'turbostratic' because they look like turbulent strata or swirling streamlines. This suggests using the concepts of hydrodynamics, viz div grad I, curl grad I, and vorticity. Alternatively, if grad I could be turned into a pseudo-velocity, it could also be turned into a pseudo displacement, and then the differential definitions of strain could be applied. There is an obvious difficulty to be overcome at this point in that the particle edges define non-directed directions.

Two of the methods extend at once to scanning electron micrographs of fractured surfaces. In many of these images, edges are bright (because electrons pass right through them), so skeletonisation is the appropriate method of edge detection. Many of these surfaces are very rough, so, on a slightly larger scale, hollows are dark and hills are bright; thus, the orientation and scale of this variability could be measured by smoothing the grey levels and segmenting at the mean grey level as described for porosity above. Fractals will also presumably be of use (see Smart and Leng, 1992). Complementary work on optical micrographs is reported by Bai *et al.* (1991) and Smart *et al.* (1992).

Conclusions

Although some work remains to be done, the methods described above have solved a problem of analysing electron micrographs of clay soils which arose thirty years ago; and preliminary results show that they can be applied to other images such as aerial photographs. Currently, micrographs are being analysed in batches of 24 or so. Intensity gradient analysis, consistency ratio mapping, porosity smoothing and segmentation, intensity gradient analysis of the porosity field, chord size analyses of both maps, and reduction of all the results for the batch are made in one run taking one hour. The computer can be left unattended during this period, but 6 versions of each image are shown to monitor the analysis; this is about one image every 30 seconds, which was the design objective. This objective was achieved without optimising the code, so it could be improved if necessary. This implementation is in Occam2 on a Meiko computer using 24 Mflops and 24 MB RAM; the image archive is 300 MB. Images are shown on a secondary monitor whilst the corresponding numerical results appear on the main screen. We understand that some of the algorithms described are available with

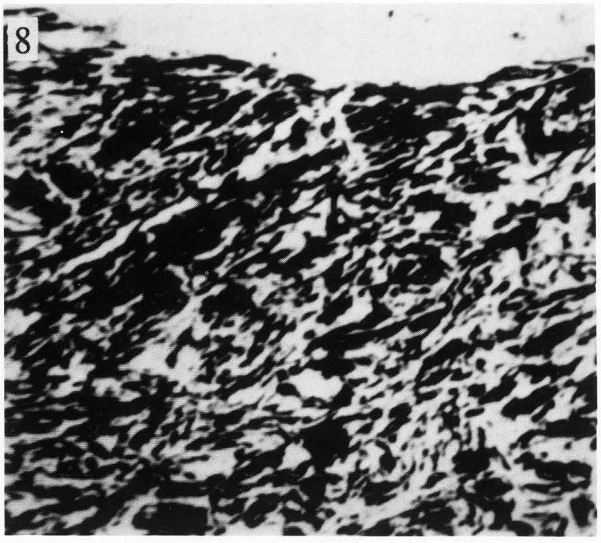

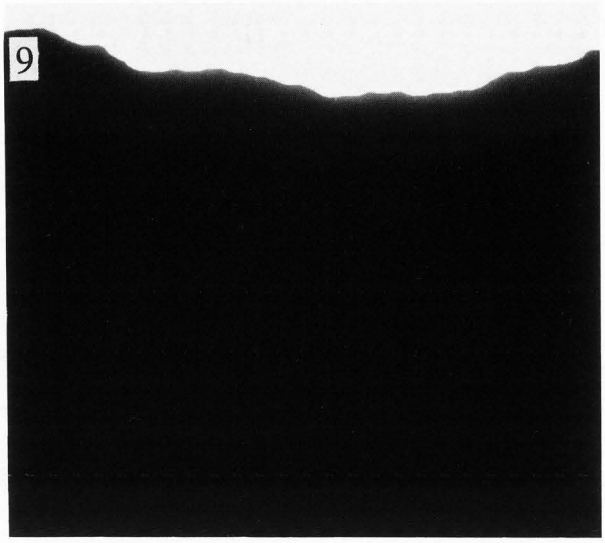

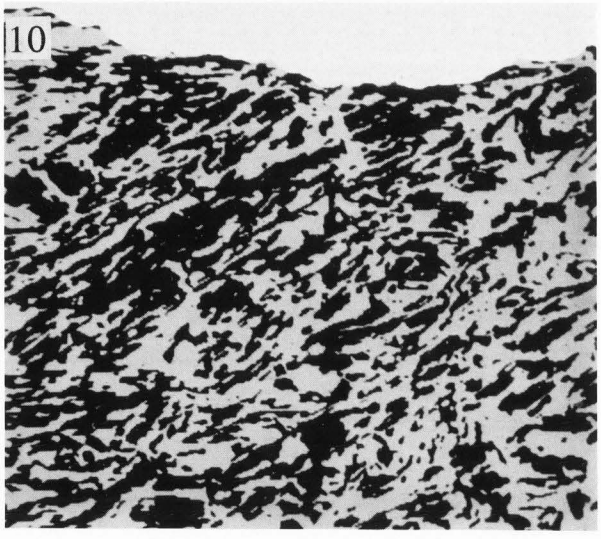

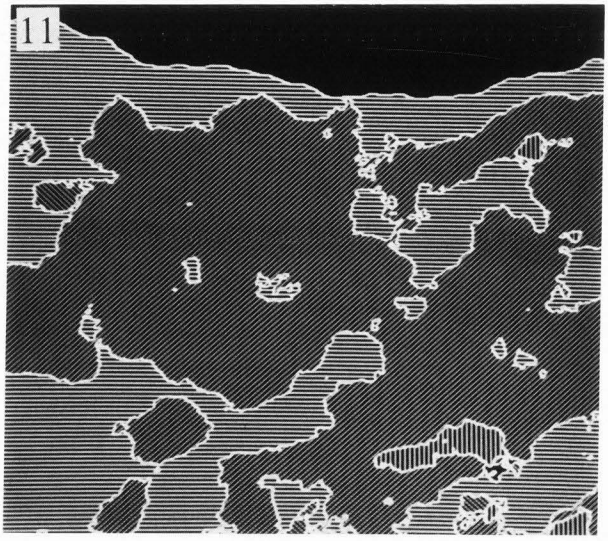

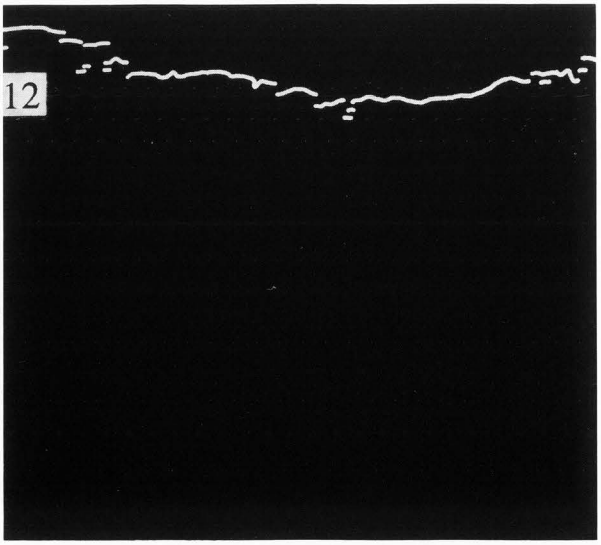

Fig. 8. Transmission electron micrograph of ultra-thin section of sheared kaolin; from Smart and Tovey, 1981. Photo width = 300 μm.

Fig. 9. Final idealised cross-section of Fig. 8 at the same magnification.

Fig. 10. Superimposition of intermediate boundary (with bumps) over the thresholded micrograph of Fig. 8 at the same magnification.

Fig. 11. Consistency Ratio Map of Fig. 8 at the same magnification; ruling indicates preferred orientation.

Fig. 12. Alternative interpretation of the surface of Fig. 8 at the same magnification.

the Semper image analysis system (Synoptics Ltd., Cambridge, England). The easiest starting point for those wishing to write their own programs is probably the Fortran code in Smart and Leng (1990b).

Acknowledgements

The work was supported by US AFOSR 97.0346 held with N.K. Tovey and M.W. Hounslow of the University of East Anglia, and by SERC TR1/099. Fig. 1 was supplied by X. Bai. Further advice was given by D. Luo, I. McConnochie, J.E.S. MacLeod, J. Kay, D. Higgins, P. Ainsworth, A. Burnett, and I. Dickson.

References

Bai X, Smart P, McConnochie I (1991). Mapping clay microstructure. Supplement to Proceedings of Royal Microscopical Society **27**(1), 19.

Bennett RH, Bryant WR, Hulbert MH (eds.) (1991). Microstructure of Fine-Grained Sediments - From Mud to Shale. Springer, New York. 582pp.

Costa L da F, Leng X, Sandler MB, Smart P (1991a). Semi-automated analysis of clay samples. Review of Scientific Instruments **62**, 2163-2166.

Costa L da F, Leng X, Sandler MB, Smart P (1991b). Analysis of clay microstructure by transputers. In: Applications of Transputers 3 - Proc. 3rd Int. Conf. Applications of Transputers, Glasgow. Durrani TS, Sandham WA, Soraghan JJ, Forbes SM (eds.). IOS Press, Amsterdam. **1**, pp. 317-322.

Derbyshire E, Unwin DJ, Fang XM, Langford M (1992). The Fourier frequency-domain representation of sediment fabric anisotropy. Computers and Geosciences **18**, 63-73.

Grabowska-Olszewska B, Osipov V, Sokolov V (1984). Atlas of the microstructure of clay soils. Panstwowe Wydawnictwo Naukowe, Warsaw. 414pp.

Grant CD, Dexter AR, Huang C (1990). Roughness of soil fracture surfaces as a measure of soil microstructure. Journal of Soil Science **41**, 95-110.

Hounslow MW, Tovey NK (1992). Porosity measurements in back scattered SEM images of particulate materials. Scanning Microscopy Supplement **6**, in press.

Leng X, Smart P (1991). Improved methods of textural analysis. In: Applications of Transputers 3 - Proc. 3rd Int. Conf. Applications of Transputers, Glasgow. Durrani TS, Sandham WA, Soraghan JJ, Forbes SM (eds.). IOS Press, Amsterdam. **1**, pp. 323-328.

Leng X, Smart P (1992). Preferred orientation in three-dimensions. Report. Administrator, Civil Engineering Department, Glasgow University, Glasgow G12 8QQ, Scotland, 8pp (available from authors).

Luo D, MacLeod JES, Leng X, Smart P (1992). Automatic orientation analysis of particles of soil microstructures. Geotechnique **42**, 97-107.

Proctor J (1977). A statistical analysis of consolidated kaolin. M.Sc. Thesis, Glasgow University.

Ross CM, Ehrlich R (1991). Objective measurement and classification of microfabrics and their relationship to physical properties. In: Microstructure of Fine-Grained Sediments - From Mud to Shale. Bennett RH, Bryant WR, Hulbert MH (eds.), Springer, New York, pp. 353-358.

Smart P (1991). Microstructural classification of clayey sediments. Geo-Marine Letters **11**, 170-171.

Smart P, Leng X (1990a). Image analysis by transputer. In: Applications of Transputers 2 - Proc. 2nd Int. Conf. Applications of Transputers, Southampton. Pritchard DJ, Scott CJ (eds.), IOS Press, Amsterdam, pp. 240-247.

Smart P, Leng X (1990b). Topcontouring programs. Report. Administrator, Civil Engineering Department, Glasgow University, Glasgow G12 8QQ, Scotland, 40pp (available from authors).

Smart P, Leng X (1991). Textural analysis by transputer - Report on SERC Transputer Loan TR1/099. SERC/DTI Transputer Loan Initiative Reports, SERC, Rutherford Appleton Laboratory, Didcot. **10**, pp. 1-15.

Smart P, Leng X (1992). Textural analysis. In: Image processing by transputer. IOS Press, Amsterdam, Chapter 4, pp. 73-95.

Smart P, Leng X, Bai X (1992). Image analysis of soil microstructure. In: Geotechnique et Informatique - Proc. International Conference on Geotechnics and Computers, Paris. Presses de l'ecole nationale des ponts et chaussees, Paris, pp. 905-912.

Smart P, Tovey NK (1981). Electron microscopy of soils and sediments: examples. Oxford University Press. 178pp.

Smart P, Tovey NK (1982). Electron microscopy of soils and sediments: techniques. Oxford University Press. 264pp.

Smart P, Tovey NK (1988). Theoretical aspects of intensity gradient analysis. Scanning **10**, 115-121.

Smart P, Tovey NK, Leng X, Hounslow MK, McConnochie I (1988). Automatic analysis of microstructure of cohesive sediments. In: Microstructure of Fine-Grained Sediments - From Mud to Shale. Springer, New York, pp. 359-366.

Tovey NK (1988). The microfabric of some Hong Kong marine soils. In: Microstructure of Fine-Grained Sediments - From Mud to Shale. Bennett RH, Bryant WR, Hulbert MH (eds.) Springer, New York, pp. 519-530.

Tovey NK, Smart P, Hounslow MW (1989a). Quantitative orientation analysis of soil microfabric. In: Proc. 8th International Working Meeting on Soil Micromorphology, San Antonio, Texas. Douglas LA (ed.), Elsevier, Amsterdam, pp. 631-639.

Tovey NK, Smart P, Hounslow MW, Leng X (1989b). Practical aspects of automatic orientation analysis of micrographs. Scanning Microscopy **3**, 771-784.

Tovey NK, Smart P, Hounslow MW, Leng X (1991). Automatic domain mapping of certain types of soil fabric. Geoderma **53**, 179-200.

Tovey NK, Smart P, Hounslow MW, Desty JP (1992). Automatic orientation analysis of microfabric. Scanning Microscopy Supplement **6**, in press.

Tovey NK, Sokolov VN (1981). Quantitative SEM methods for soil fabric analysis. Scanning Electron Microscopy **1981**;I, 536-554.

Unitt BM (1975). A digital computer technique for revealing directional information in images. Journal of Physics E **8**, 423-425.

Webster R, Oliver MA (1990). Statistical methods in soil and land resource survey. Oxford University Press. 316pp.

Discussion with Reviewers

Reviewer II: Could the limitations of field of view be overcome by combining results of several images?
Authors: In theory, yes; but at the moment we lack the software to patch the images together.

Reviewer II: Was the electrical interference a changing effect or related to the digitisation?
Authors: There was a problem in the digitisation. We think that an electromagnetic field set up by the power supply distorted the analogue signal flowing to the A/D converter. These were some charging effects on the sample; but the intensity gradient approach is relatively insensitive to these.

Reviewer II: What was the thickness of the ultra-thin section in Fig. 8?
Authors: Nominally 40 nm.

Reviewer II: Why are edges bright in scanning electron micrographs?
Authors: On a flat surface, all of the incident electrons burrow into the material and only those which are completely turned round escape back towards the collector; at an upstanding edge, all of the electrons are available for collection except those which are turned downwards into the bulk material.

Reviewer II: Two-dimensional Fourier transforms give directional information. Could the authors comment on the applicability of fast Fourier transforms for orientation analysis in comparison to intensity gradient analysis?
Authors: The most successful use of Fourier transforms which we have seen for this purpose is Derbyshire *et al.* (1992).

Reviewer II: Do the authors think it will be practical to explore the three dimensional structure of thin sections of soil using the TEM with electron tomography?
Authors: This is an interesting suggestion which we would like to see assessed. It might be necessary to use a high voltage transmission electron microscope and very thin sections; ultra-thin sections might not contain enough information in the third dimension.

P.W. Hawkes: Please explain the concept of semi-variograms?
Authors: Let Pi,j be the i-th pixel of the j-th row, and let $I(i,j)$ be its intensity. Then, the semivariance, $g(p,q)$ of an image of size (l,m) can be defined as:

$$g(p,q) = \frac{1}{2(l-p)(m-q)} \sum_{i=1}^{l-p} \sum_{j=1}^{m-q} [I(i,j)-I(i+p,j+q)]^2$$

Thus, $g(p,q)$ measures the average difference of all pairs of pixels which are separated by the vector (p,q). The vector (p,q) is known as the lag; and the three-dimensional graph of $g(p,q)$ vs. p and q is known as the semi-variogram. The semi-variance is zero at the origin, increases as the lag increases, and usually flattens out on a plateau far from the origin. In simple cases, the semi-variance is constant for all lags greater than a certain size, which is known as the range. The range, may vary with direction. In this case, the relationship between any two pixels which are further apart than the range is random. However, if there is long-range order in the sample, this will be evident as waves in the outer portion of the semi-variogram (see Smart and Leng, 1992). In some cases, the semi-variance at very small lags, i.e., 1 pixel upwards, is significantly greater than zero. In these cases, a right-cone through a three-dimensional graph in this region (excluding the point at the origin) will extrapolate to $g'(0,0) > 0$. This extrapolated value, $g'(0,0)$, is called the nugget variance.

G. Bonifazi: Could the authors provide flow charts describing the strategy and basic assumptions adopted?
Authors: The clearest way of answering this question will be to give a simplified description of the main program which we supplied to one of our colleagues (the actual program consists of 7 main processes and 12 communications processes running in parallel on 6 processors). Before this program is run, all the images have been checked and put into order, and all the parameters such as radius of filter have been agreed. Then, the principal steps are:

1. Read an image.
2. Find the intensity gradient, A and U, over the whole image, Equations (2) and (3).
3. Use the consistency ratio filter to smooth the intensity gradient and find R, C, and T, Equations (8)-(11).
4. Smooth the intensity and then convert to porosity, p, Equation (12).
5. Find the intensity gradient over the smoothed porosity image, c.f. Equations (2) and (3) which now apply to p.
6. Segment the image containing the smoothed angle, T, into the desired number of directions (and random areas); measure horizontal and vertical chords.

7. Segment the smoothed porosity image at the porosity obtained by gravimetric analysis; measure horizontal and vertical chords.

During these seven stages, the original image, the image of U, and the two segmented images are displayed in turn; and a lot of histograms are collected.

8. From the histograms, calculate three consistency ratios for the whole image based on:

8a. the raw intensity gradient, Step 2;

8b. the smoothed directional field, Step 3;

8c. the intensity gradient of the porosity field, Step 5.

9. Add the histograms for the image to the histograms for the batch of images.

10. Loop back to Step 1 until all images of the batch have been completed.

11. Repeat Step 8 using the histograms for the whole batch; and calculate means and standard deviations of all the scalars.

12. Present selected histograms on the screen for inspection.